

New routes to organometallic molecular junctions via a simple thermal processing protocol†

Ruben Ezquerra,^a Samantha G. Eaves,^{c,d} Sören Bock,^c Brian W. Skelton,^c Francesc Pérez-Murano,^e Pilar Cea,^{a,b,f*} Santiago Martín,^{a,f*} Paul J. Low^{c*}

^a Departamento de Química Física, Facultad de Ciencias, Universidad de Zaragoza, 50009, Spain. Email pilarcea@unizar.es

^b Instituto de Nanociencia de Aragón (INA) and Laboratorio de Microscopías Avanzadas (LMA), edificio i+d Campus Rio Ebro, Universidad de Zaragoza, C/Mariano Esquillor, s/n, 50018 Zaragoza, Spain

^c School of Molecular Sciences, University of Western Australia, 35 Stirling Highway, Crawley, WA, 6009, Australia. Email paul.low@uwa.edu.au

^d Department of Chemistry, Durham University, South Rd, Durham, DH1 3LE, UK

^e Instituto de Microelectrónica de Barcelona (IMB-CNM, CSIC) Campus UABBellaterra 08193, Spain

^f Instituto de Ciencias de Materiales de Aragón (ICMA), Universidad de Zaragoza-CSIC, 50009 Zaragoza, Spain. Email smartins@unizar.es

† This paper is dedicated to Professor Martin R. Bryce, friend and mentor, in recognition of his many outstanding contributions that have advanced the field of molecular materials science.

Abstract

Methods for forming single- and multiple-molecule junctions are key to the development of molecular electronics and the further study of allied electronic and electrical properties of molecules arising from through-molecule charge transport. The organometallic complex *trans*-Ru(C≡C-3-C₄H₃S)(C≡C-1,4-C₆H₄C≡CAuPPh₃)(dppe)₂ forms well-ordered, densely packed self-assembled monolayers on gold and silver substrates, contacted through the sulfur atoms of the thiophenyl groups. Upon mild thermal treatment (150 – 200 °C, two hours) the gold moiety decomposes to liberate PPh₃ and form quite uniform, disc-

shaped gold nanoparticles on top of the organometallic monolayer. The resulting molecular junctions give rise to sigmoidal shaped I - V curves characteristic of through-molecule conductance, rather than linear, ohmic traces associated with metallic contacts (i.e. short circuits). This work therefore demonstrates the feasibility of thermal processing routes to form good quality molecular junctions from organometallic complexes of relatively complex molecular structure capped with uniformly-shaped nanoparticles formed in situ.

Introduction

The field of molecular electronics has advanced rapidly in recent years through the advent of a range of experimental methods for the construction of single- and multiple-molecule molecular junctions (i.e. electrode | molecule(s) | electrode structures).¹⁻⁴ The characterisation of the electrical properties of the molecules within the junction under a wide range of conditions has led to advances in our understanding of molecular conductance, and related transport phenomena.⁵⁻⁷ In turn, this understanding opens opportunities for the development of device concepts with properties that are difficult or impossible to achieve with conventional materials.⁸ Whilst single molecule junctions allow intricate details of the molecular junction structure to be explored and chemical structure to be correlated with transport properties,⁷⁻¹⁰ large area junctions represent a more realistic practical device configuration.^{11, 12}

Single-molecule junctions are now relatively simple to construct using mechanically controlled break junction (MCBJ)¹³ and closely related STM break junction (STM-BJ) techniques, as well as allied STM-based methods such as the current-distance ($I(s)$)^{14, 15} and current-time or telegraphic blinking ($I(t)$)¹⁶ techniques.¹⁰ Multiple-molecule junctions are typically constructed via the introduction of a 'top contact' electrode onto a molecular monolayer. Examples include cross-bar junctions, nanoparticle-capped nanopores, the use of liquid metal^{17, 18, 30-33} and eutectic metal alloy top electrodes,^{19, 34} and deposition of pre-formed metal nanoparticles onto a monolayer bearing a suitable ligating functional group on the exposed top surface.^{20, 21} However, the cross-bar

junctions are experimentally demanding, and liquid metal or eutectic electrodes are not likely to translate to device structures. The use of nanoparticle top contacts to give electrode | molecule | nanoparticle junctions has been widely explored, and the use of such nanoparticle junctions in the construction of a molecular-monolayer memory device has been recently described.²² Strategies to these structures include direct deposition²³ or growth²⁴ of naked metal nanoparticles onto monolayers bearing an exposed functional group on the top surface capable of ligating to the nanoparticle, and electrochemical deposition of metal particle seeds on top of a monolayer prior to electroless metal in-fill.²⁵ As an alternative to electrochemical reduction, photochemical reduction of AuCl₄⁻ or Ag⁺ ions co-deposited on the top-surface of a Langmuir-Blodgett monolayer gives rise to high surface coverage of the monolayer by Au²⁶ or Ag²⁷ nanoparticles.

We have recently described a 'soft', thermal method for the fabrication of gold nanoparticles on an organic monolayer film.²⁸ In early work, Coco, Espinet and colleagues demonstrated that metallic gold nano-particles (GNPs) could be formed by thermolysis of alkynylisocyanide gold complexes, Au(C≡CC₆H₄C_mH_{2m+1})(CNC₆H₄OC_nH_{2n+1}), in solution or directly from a mesophase,²⁹ and deposited on the inner and outer surfaces of carbon nanotubes.³⁰ By modifying the gold(I) complex to introduce a suitable moiety capable of acting as a surface anchor group, such as the aniline fragment in [(MeOC₆H₄-4-N≡C)Au(C≡CC₆H₄-4-NH₂)], it is possible to immobilise the complex on an electrode substrate via the Langmuir-Blodgett technique, forming a well-packed, directionally orientated monolayer.²⁸ The modified substrate is then annealed in order to simultaneously break the bonds to the ancillary ligands, and reduce Au(I) to Au(0), presumably in concert with oxidation of the liberated ancillary ligand(s), resulting in the formation of gold nano-particles (GNPs) on the surface of the monolayer, establishing the Au|monolayer|Au junction. This Thermally Induced Decomposition of an Organometallic Compound (TIDOC) method was found to be effective at moderate temperatures (150 – 200 °C for two hours), with the electrical properties of the resulting Au|molecule|GNP junctions being characterised by the usual sigmoidal *I-V* curve

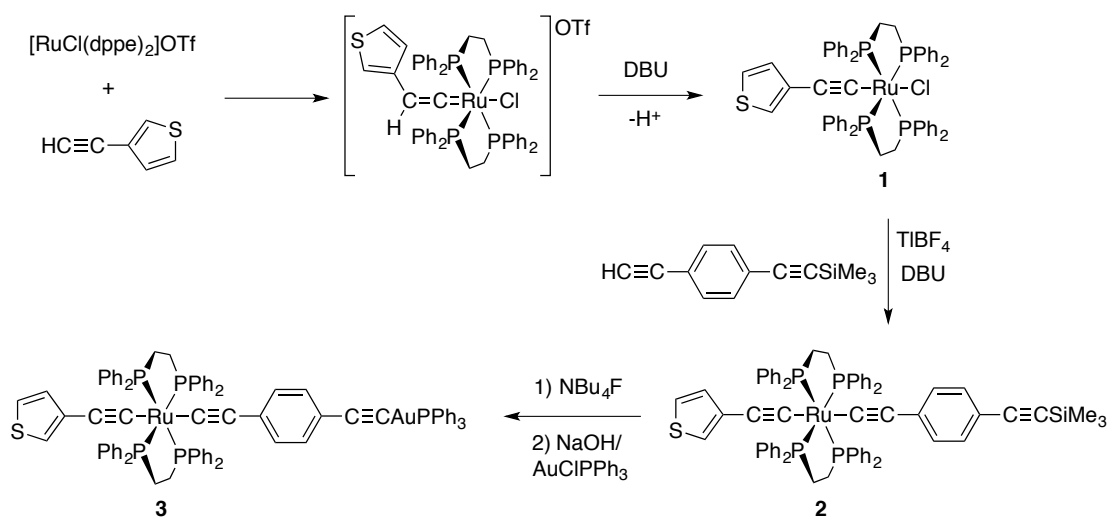
that signifies a molecular junction, as opposed to metallic contact. The molecular design strategy could also be extended to phosphine complexes, such as $\text{Au}(\text{C}\equiv\text{CC}_6\text{H}_4\text{C}\equiv\text{CC}_6\text{H}_4\text{CO}_2\text{H})(\text{PPh}_3)$ with similar results.²⁸

Although the field of molecular electronics has been advanced through the construction and study of molecular junctions featuring organic compounds, the electrical characteristics of single-molecule junctions formed from inorganic complexes and organometallic molecules have begun to attract increasing attention.³¹⁻³⁵ The growing interest in metal-complex based molecular electronics has also prompted studies of metal complexes within, for example, 'large area' c-AFM,³⁶ cross-bar³⁷ and eGaIn junctions,³⁸⁻⁴⁰ as well as nanofabricated device platforms.⁴¹⁻⁴⁵ This increasing activity is due to the potential that metal complexes offer for not only improving the alignment of critical frontier molecular orbitals with the electrode Fermi levels to increase molecular conductance,⁴⁶ but also the potential to exploit the unique redox, magnetic and photochemical properties of metal complexes to engineer electrical characteristics within the junction that cannot be achieved with purely organic compounds.

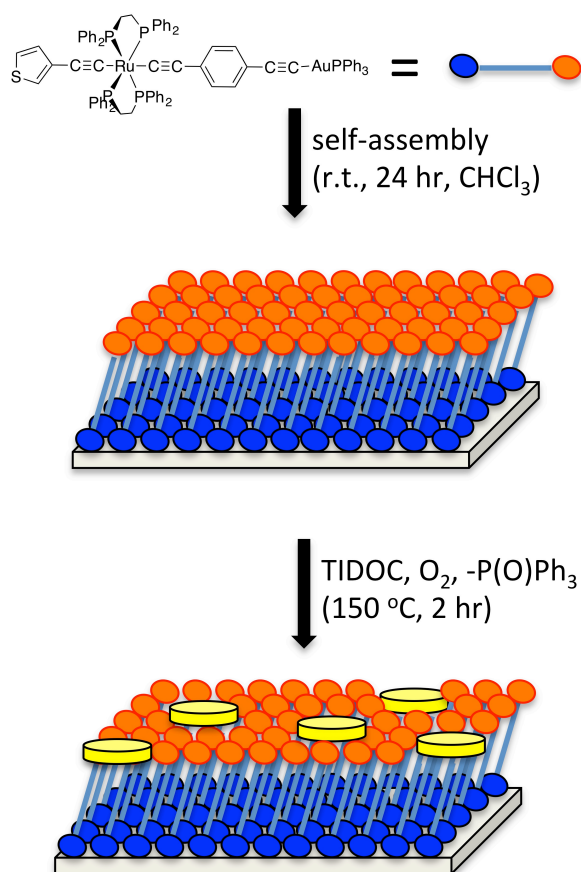
The promising electrical behaviour of metal bis(acetylide) complexes in single molecule⁴⁷⁻⁵³ ^{46, 54-58} and large area^{36, 37, 59, 60} junctions now prompts us to further examine the TIDOC method with such compounds. Here we demonstrate an exceptionally facile fabrication route to electrode|organometallic complex|nanoparticle junctions, by mild thermal processing of self-assembled monolayers of *trans*- $\text{Ru}(\text{C}\equiv\text{C}-3\text{-C}_4\text{H}_3\text{S})(\text{C}\equiv\text{C}-1,4\text{-C}_6\text{H}_4\text{C}\equiv\text{CAuPPh}_3)(\text{dppe})_2$. The resulting highly monodisperse, disc-shaped (ca. 20 x 2 nm) nanoparticles, which are electrically well connected to the underlying organometallic monolayer, are prepared without use of additional ligands to moderate growth, control pH or special effort to control the reaction conditions. These results therefore allow the simple construction of nanoparticle-capped molecular junctions from a single chemical precursor.

Results and Discussion

The synthesis of *trans*-Ru(C≡C-3-C₄H₃S)(C≡C-1,4-C₆H₄C≡CAuPPh₃)(dppe)₂ (**3**) which features both a 3-thienyl surface contacting or anchor group,^{55, 61} a wire-like *trans*-Ru(C≡CR)₂(dppe)₂ core^{32, 46, 55, 57} and the C≡CAuPPh₃ fragment as the TIDOC precursor,²⁸ is summarised in Scheme 1. The complete TIDOC process is summarised in Scheme 2, and individual steps are discussed further below.



Scheme 1. An illustration of the preparation of compound **3**, showing the relevant intermediates.



Scheme 2. A schematic representation of the TIDOC based preparation of 'organometallic' molecular junctions.

Synthesis and characterisation

The reaction of the five-coordinate complex $[\text{RuCl}(\text{dpppe})_2]\text{OTf}$ with 3-ethynylthiophene, $\text{HC}\equiv\text{C}-3-\text{C}_4\text{H}_3\text{S}$, gave the monoacetylide complex *trans*- $\text{RuCl}(\text{C}\equiv\text{C}-3-\text{C}_4\text{H}_3\text{S})(\text{dpppe})_2$ (**1**) after deprotonation of the intermediate vinylidene.⁶²⁻⁶⁴ Further reaction of **1** with $\text{HC}\equiv\text{C}-1,4-\text{C}_6\text{H}_4\text{C}\equiv\text{CSiMe}_3$ in the presence of TlBF_4 , to abstract the chloride ligand, and DBU, to deprotonate the intermediate vinylidene,⁶⁵ gave *trans*- $\text{Ru}(\text{C}\equiv\text{C}-3-\text{C}_4\text{H}_3\text{S})(\text{C}\equiv\text{C}-1,4-\text{C}_6\text{H}_4\text{C}\equiv\text{CSiMe}_3)(\text{dpppe})_2$ (**2**, 75%). Finally, desilylation of **2** (NBu_4F)⁶⁵ and auration ($\text{NaOH} / \text{AuCl}(\text{PPh}_3)$)⁶⁶ afforded the bimetallic complex **3** (84%). The complexes **2** and **3** were characterised by the usual array of multinuclear NMR spectroscopies, mass spectrometry, IR spectroscopy and elemental analysis. In addition, a crystal of **2** suitable for X-ray diffraction was obtained, allowing

determination of the molecular structure, details of which are provided in the Supporting Information.

Self-assembled monolayer (SAM) formation and characterisation

To form and monitor SAM deposition from **3**, a gold quartz crystal microbalance (QCM) substrate was incubated for 24 hours in a 10^{-4} M solution of the complex in chloroform. After this time no further frequency variation was observed. The surface coverage of the resulting organometallic monolayer was determined to be 1.7×10^{-10} mol·cm⁻², from the observed frequency variation of -30 Hz and the relationships described by the Sauerbrey equation,⁶⁷

$$\Delta f = -\frac{2 \cdot f_0^2 \cdot \Delta m}{A \cdot \rho_q^{1/2} \cdot \mu_q^{1/2}} \quad (1)$$

where: Δf = frequency variation before and after deposition of the monolayer; f_0 = fundamental resonant frequency of ca. 5 MHz; Δm = mass change; A = electrode area; ρ_q = density of the quartz (2.65 g·cm⁻³) and μ_q = the shear module (2.95×10^{11} dyn·cm⁻²).

The experimental value of the surface coverage is in good agreement with that estimated from the effective molecular area determined by the molecular modelling program (Spartan 08 V 1.0.0) (2.4×10^{-10} mol·cm⁻²), and therefore consistent with monolayer formation.

In order to determine the nature of the interaction between **3** and the gold substrate, and hence gain information about the molecular orientation and order in the film, XPS measurements were carried out on both a powdered sample of **3** and a SAM of **3** on gold (Figure 2).⁶⁸ Due to spin-orbit splitting, the XPS spectrum of the powder in the S(2p) region gives 2p_{3/2} and 2p_{1/2} peaks, falling at 163.9 and 165.1 eV, with an area ratio of 2:1.⁶⁹ In the XPS spectrum of the SAM of **3**, these spin-orbit split peaks appear at 161.8 and 163.1 eV. The decrease in the S(2p) binding energy is indicative of an interaction between the sulfur atom and the gold surface,⁷⁰ suggesting that compound **3** interacts with the gold substrate

through the 3-thienyl group. In addition, the XPS spectra of the SAM of **3** in the P(2p) and Ru(3d) regions do not show any significant changes in the binding energy of the peaks compared to the powder XPS spectrum (Figure 2) indicating that compound **3** remains intact after being grafted onto the gold surface.

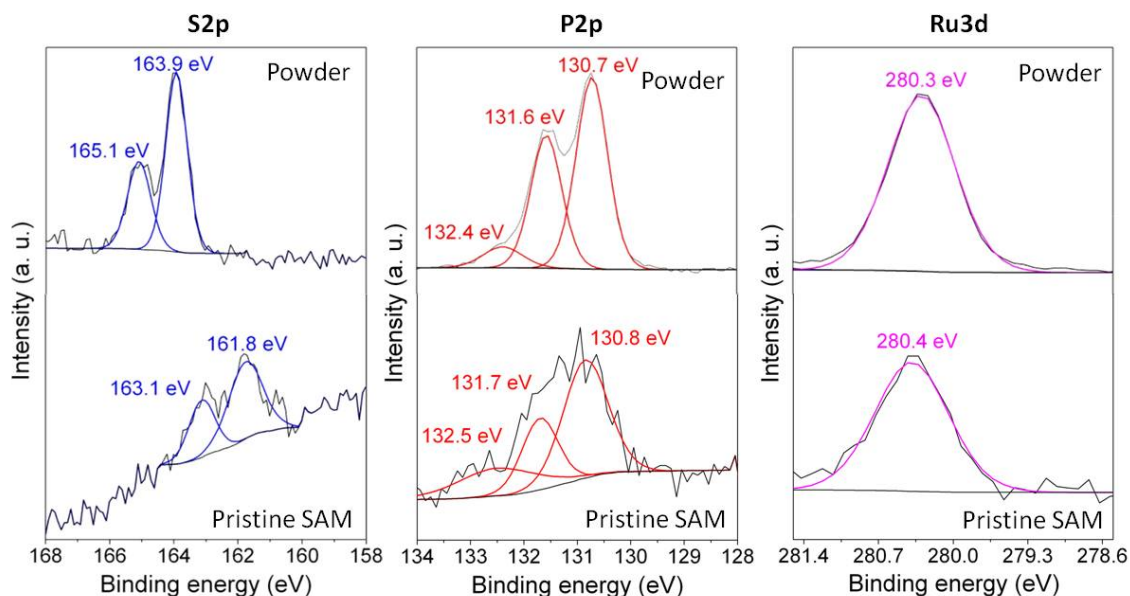


Figure 2. XPS spectra of S(2p), P(2p) and Ru(3d) photoelectrons of compound **3** in powder and as a self-assembly monolayer (SAM) on a gold substrate. (Note: to clarify, in the Ru spectra, only the Ru(3d_{5/2}) peaks are shown due to the very strong overlap between the Ru(3d) and C(1s) regions).

TIDOC studies

In a manner similar to that reported earlier for TIDOC studies with gold-functionalised organic monolayers,²⁸ a monolayer film of the organometallic complex **3** on a gold QCM substrate was annealed at 150 °C for two hours, and subsequently rinsed copiously with chloroform to remove any physisorbed material, and dried under a stream of dry N₂. Assuming that the surface coverage of the organic monolayer is maintained after the annealing, washing and drying process, the change in frequency (6 Hz) observed corresponds to a loss of a material of 262 amu, i.e. triphenyl phosphine (PPh₃).

In related studies, the thermal decomposition of gold complexes Au(C≡CR)(CNR') to give gold nanoparticles in solution has been proposed to proceed via

aggregation through aurophilic Au...Au interactions, and oxidative coupling of the alkynyl ligands associated with the reduction of Au(I) to Au(0).²⁹⁻³⁰ In the present case, the steric bulk of the PPh₃ ligands prevents aurophilic interactions, as demonstrated by various explorations of solid-state structures.⁷¹ However, *in situ* reduction of phosphine-stabilised gold complexes in solution, in hydrogels or on a variety of templates to give nanoparticles is also known.⁷²⁻⁷⁷ In the present case, in the absence of a specific reducing agent we speculate that the reduction of Au(I) is initiated by oxidation of the PPh₃ ligands.

XPS spectra were also recorded from a SAM of **3** supported on a silver substrate, chosen to avoid any misinterpretation of the results, particularly in the Au(4f) region, from an underlying gold substrate. The XPS spectrum of the pristine SAM of **3** on a silver substrate in the P(2p) region (Figure 3) shows a doublet peak due to the spin-orbit splitting effect at 130.8 and 131.7 eV corresponding to the 2p_{3/2} and 2p_{1/2} peaks and attributed to the dppe ligand, as well as a peak at 132.5 eV due to the phosphorus contained within the triphenylphosphine (PPh₃) ligand. The area ratio of 4:1 for the peaks attributed to the dppe and PPh₃ ligands is consistent with the stoichiometry of complex **3**. After the silver-supported SAM was annealed for 2 hours at 150 °C to initiate the TIDOC process, the characteristic phosphorus peaks of the PPh₃ group are absent, indicating the loss of the triphenylphosphine ligand. In addition, whilst the Au(4f) region for the pristine monolayer on silver shows two peaks at 88.6 and 85.0 eV, attributed to Au(I),^{28,78} and two weaker peaks at 87.4 and 83.5 eV, attributed to Au(0) formed by action of the incident X-ray beam on the sample, the SAM after the annealing process shows only peaks characteristic of Au(0) at 87.4 and 83.7 eV.^{28,79}

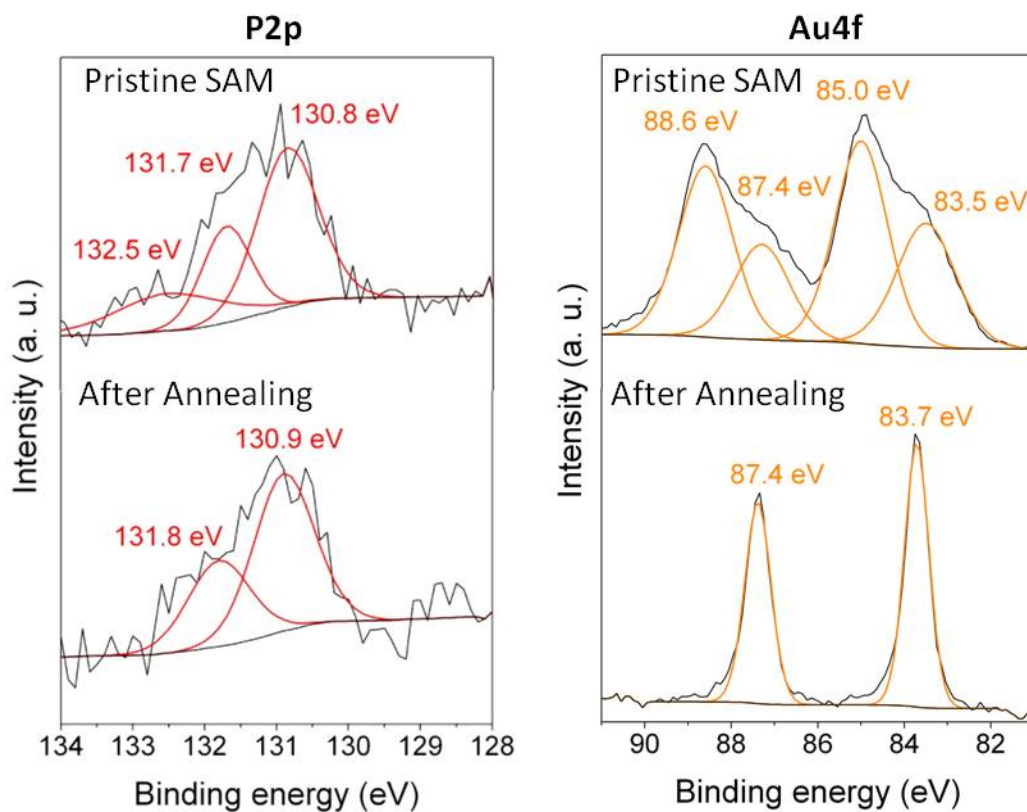


Figure 3. XPS spectra of P(2p) and Au(4f) photoelectrons of a pristine SAM of **3** onto a silver substrate , after annealing at 150 °C for 2 hours.

To obtain information about the distribution of the metallic gold detected by XPS, the monolayer was imaged using atomic force microscopy (AFM) before and after the annealing process (Figure 4). In contrast to the smooth and featureless surface exhibited by a pristine SAM of **3** (surface roughness, calculated in terms of the Root Mean Square (RMS), 0.3 ± 0.1 nm), after annealing, the root mean square (RMS) roughness of the SAM increases (up to 1.13 ± 0.2 nm). The bright spots distributed over the film surface in the AFM image indicate the presence of GNPs.

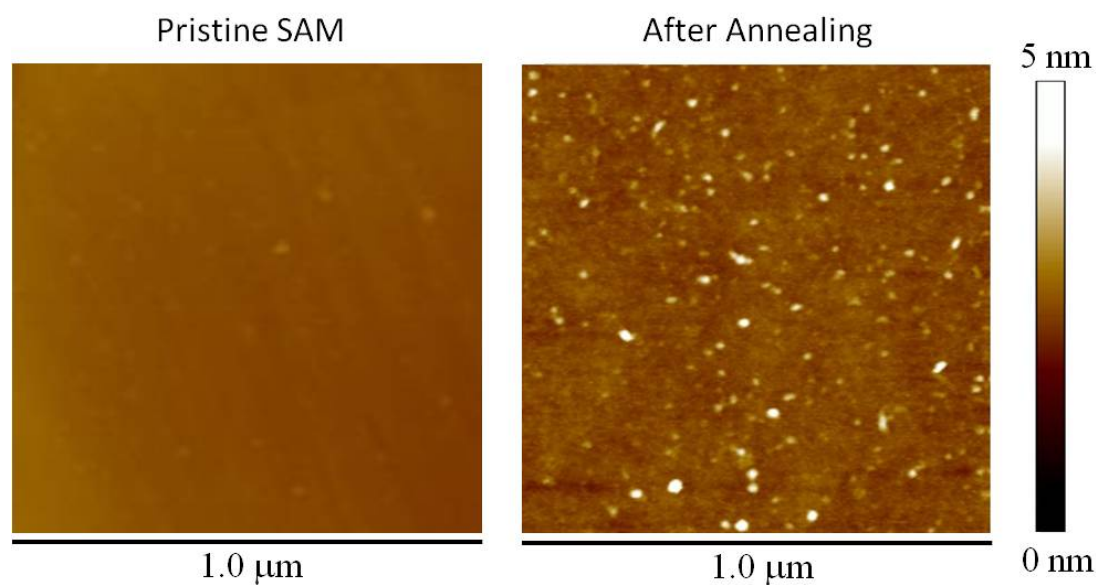


Figure 4. AFM images of a SAM of **3** on a gold substrate (left) and after annealing the same SAM for two hours at 150 °C (right).

Height profiles across AFM images over ca. 65 individual particles were used to determine both diameters and heights of GNPs (Figure 5). The statistical analysis of the data extracted from AFM images revealed that these GNPs exhibit an average diameter of around 20 nm (corrected by the tip convolution)⁸⁰ and an average height of ca. 2.6 nm. Histograms illustrating the diameter and height value distributions are given in Figure 5c and 5d, respectively.

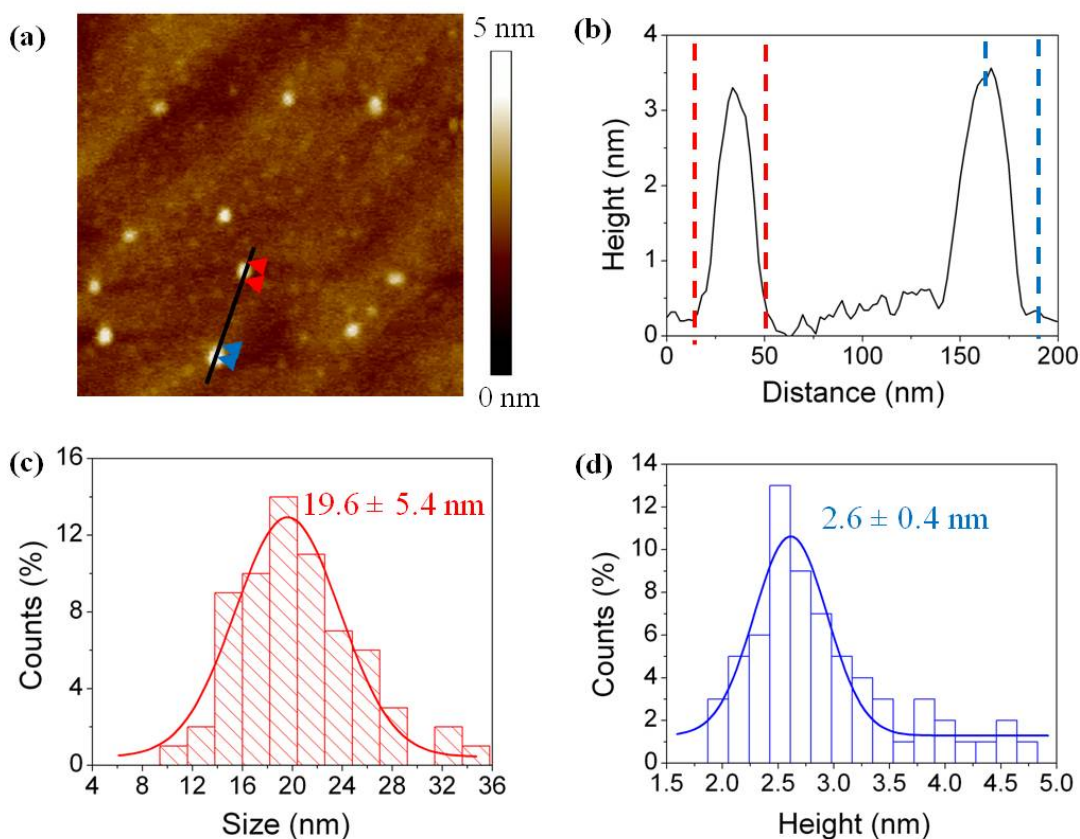


Figure 5. (a) 550x550 nm² AFM image of a SAM of **3** after annealing showing the presence and distribution of gold nanoparticles used in the accompanying analysis. (b) Representative cross section and analysis profile illustrating the dimensions of the measured GNPs. Histograms showing the particle size (corrected by the tip convolution), red line, and height distributions, blue line, corresponding to 65 GNPs from different AFM images, (c) and (d), respectively. Averaged NPs diameter and height values are showed in their respective graphs.

In order to calculate the surface coverage by the TIDOC generated gold nanoparticles, a bearing analysis of the AFM images was made. In this analysis, the depths of all pixels of the image with respect to a reference point, i.e., the highest pixel, are analyzed to give an estimation of the percentage of area covered by features, i.e. surface coverage, at every pixel depth. The analysis of a coverage data recorded over 1x1 μm² area indicates an average GNP-coverage of ca. 20% (Figure 6).

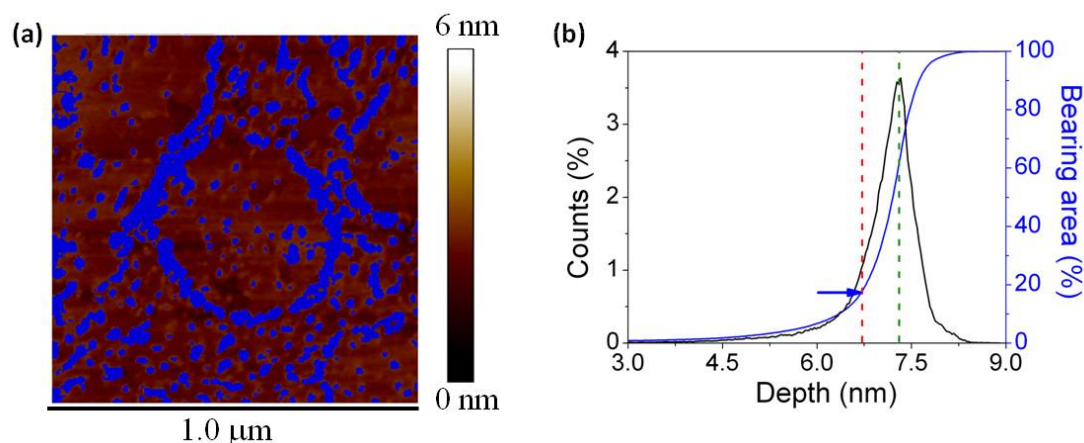


Figure 6. (a) $1 \times 1 \mu\text{m}^2$ AFM image of a SAM of **3** after annealing with the mask in blue indicating nanoparticle-free areas. (b) Depth histogram showing the distribution of height data at different depth referred to a reference point, i.e. the highest pixel (black line). The blue line (bearing analysis) indicates the relative projected area covered at each depth value depicted as a blue mask in the topographic image. The peak in the histogram marked with a green-dashed vertical line is attributed to the nanoparticle-free molecule-modified substrate while the red line accounts for the selected height threshold corresponding to the lowest maximum peak associated with the height of the measured GNPs.

Electrical characterisation of molecular junctions formed by TIDOC

Assuming the organometallic molecular core remains intact after the TIDOC process, a suggestion which is consistent with the P(2p) XPS spectra, the TIDOC-formed GNPs mark the location of $\text{Au}_{\text{substrate}}|[(\text{SC}_4\text{H}_3\text{-3-C}\equiv\text{C})\{\text{Ru}(\text{dppe})_2\}(\text{C}\equiv\text{CC}_6\text{H}_4\text{C}\equiv\text{C})]_x|\text{GNP}$ molecular junctions featuring one or more organometallic fragments. The electrical characteristics of these GNP-capped junctions were assessed from the sigmoidal-shaped current-voltage (I - V) curves collected using a conducting-AFM (Bruker ICON) operating in the Peak Force Tunneling AFM (PF-TUNATM) mode. The I - V measurements were repeated many times and the conductance values were obtained from the slope of the linear fit of the average I - V curve in the ohmic region (ca. -0.3 to 0.3 V in this case). The intermittent contact between the AFM tip and the surface at a frequency of 2 kHz, a low maximum normal force (peak-force) and limited lateral forces associated

with PF-TUNA™ are chosen to limit physical damage to the surface by the tip during measurement.^{27, 28, 81 82} Nevertheless, before registering the *I-V* curves by locating the AFM tip on top of a GNP, the most suitable contact force to be applied during the measurement has to be selected, allowing for the ca. 8% uncertainty in the set-point force due to the calibration method (thermal tuning).⁸³ If the initial set-point force is too great, the tip will cause an unacceptably large deformation of the SAM underlying the GNPs. Conversely, if the set-point force is too low, there will be inadequate electrical contact between the AFM probe tip and the GNP.

A region of the TIDOC processed film on Au(111) featuring three clearly defined GNPs was chosen to explore and determine the range of appropriate set-point forces (Figure 7a, inset). At set-point forces between 1–3 nN, the section analysis for each of the three isolated GNPs gives essentially a constant height, indicating that no significant deformation of the monolayer occurs and that the GNPs are not substantially pushed into the monolayer by the AFM tip (Figure 7a). However, at these set-points, practically no current was detected through the junction, indicating poor electrical contact between the tip and the nanoparticle. When the set-point force was increased to 5 nN, the section analysis of these nanoparticles gave only a ca. 10% decrease in the relative height of the GNPs, but now a significant conductance through the junction could be measured; in other words, at 5 nN set-point, there is a good electrical contact between the tip and the nanoparticle without substantial deformation of the underlying molecular layer. Further increasing the set-point force between 10-20 nN resulted in steadily lower height values and higher junction conductance (Figure 7a).

Taking 5 nN as the set-point at which good electrical contact is achieved with minimal deformation of the underlying layer, *I-V* curves (ca. 100) were recorded after locating the AFM tip on top of different nanoparticles and sweeping the tip voltage (± 1.0 V) with the Au substrate held at ground (Figure 7b). In each case, the *I-V* curve featured the characteristic sigmoidal shape associated with molecular conductance, rather than linear, ohmic traces that would indicate metallic contacts and hence short-circuits through the junctions. From the

average I - V curve, a junction conductance of $1.6 \times 10^{-4} G_0$ was determined. Although the precise number of molecules within each junction cannot be determined, we note that this value is in a similar range to the ‘low conductance’ value determined from single molecule junctions of the related complex *trans*- $\text{Ru}(\text{C}\equiv\text{C}-3-\text{C}_4\text{H}_3\text{S})_2(\text{dppe})_2$.⁵⁵

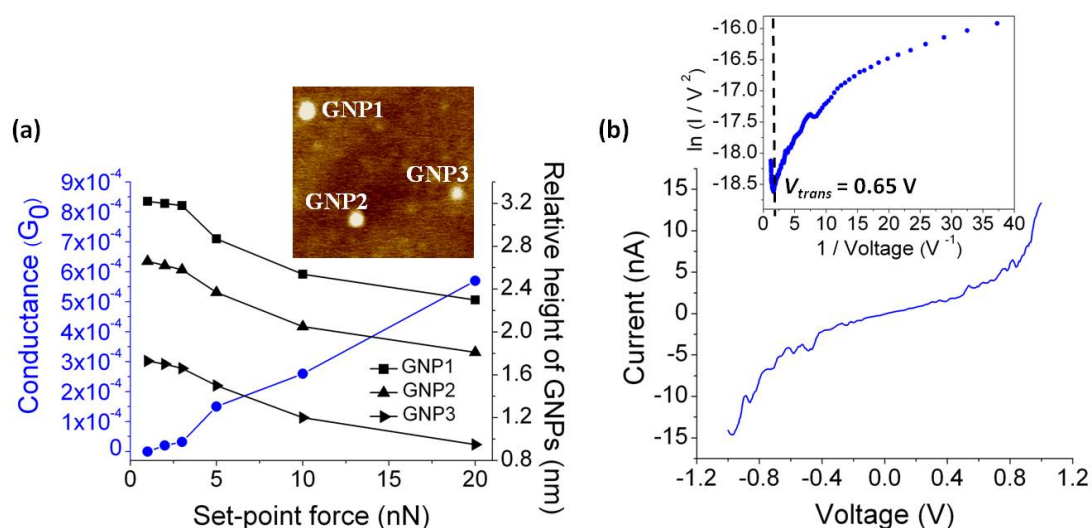


Figure 7. (a) Relative height of three GNPs determined with the c-AFM at the indicated set-point forces to study the deformation of the monolayer as a function of the set-point force together with the average conductance values (determined from the linear section (-0.3 to $+0.3 \text{ V}$ range) in the recorded I - V curve) measured by locating the tip of the c-AFM on top of GNPs as these showed in the $300 \times 300 \text{ nm}^2$ AFM image. (b) Average I - V curve experimentally obtained by positioning the c-AFM tip on top of a GNP when a set-point force of 5 nN was applied. Inset: a Fowler-Nordheim plot for the average I - V where the transition voltage is marked.

Finally, transition voltage spectroscopy (TVS) was used to determine the transition voltage (V_{trans}) from the inflection behaviour in the Fowler-Nordheim plot (Figure 7b inset). It is often assumed that this inflection occurs when a frontier molecular orbital level (HOMO or LUMO) substantially responsible for electrical transmission through the molecular junction approaches the Fermi level of the electrodes.⁸⁴ In such cases, lower V_{trans} values imply a better

alignment between the metal Fermi level and the frontier molecular orbitals and V_{trans} gives a measure of the tunnel barrier height.⁵⁴ However, the dependence of the term on other factors including molecular length (i.e. tunnel barrier width), chemical nature of the electrode-molecule contact and electrode material, and the significance to various tunneling models has been discussed, and the idea of V_{trans} as a measure of the non-linearity of bias dependent conductance proposed.⁸⁵ Therefore a direct comparison of values between chemically distinct systems is potentially fraught, despite the popularity of the approach, and for molecules of different chemical composition, it is unlikely that V_{trans} can be used as an independent parameter concerning the 'superiority' of one compound over another. There are few V_{trans} measurements from organometallic compounds reported to date, and the value determined here (0.65 V) can only be compared with that determined from similarly structured bis(thiolate) contacted *trans*-Ru(C≡CC₆H₄-4-S)₂(dppm)₂ (0.25 V).⁴⁷ It is likely that the differences in absolute value reflect the different contacting groups and tunnel barrier length as much as energy level alignment.

Conclusion

The development of methods that allow the formation of molecular junctions and hence the experimental determination of the electrical characteristics and properties of single molecules has provided enormous impetus to the field of molecular electronics. However, the translation from single-molecule junctions to 'large area' devices has been complicated by the difficulties in forming electrode contacts on top of monolayers of molecules. The use of gold nanoparticles (GNP) as nascent 'top electrode' contacts and as buffer layers in the fabrication of molecular electronic devices inspires further exploration of routes to prepare GNP based molecular junctions. The heterobimetallic complex *trans*-Ru(C≡C-3-C₄H₃S)(C≡C-1,4-C₆H₄C≡CAuPPh₃)(dppe)₂ gives rise to well-ordered, densely-packed monolayers of a 'wire-like' organometallic ruthenium complex from a simple self-assembly method, taking advantage of the thienyl sulfur-gold interaction. Subsequent thermal decomposition of the 'TIDOC' ethynyl(triphenylphosphine)gold head-group provides a simple route to GNP-

capped organometallic molecular junctions with good electrical properties. This work demonstrates that organometallic ruthenium bis(acetylide) complexes, which have been identified as a promising molecular substructure for use in molecular electronics, are compatible with mild thermal processing routes, allowing both the further exploration of the electrical properties of these systems and demonstrating the feasibility of incorporating such systems into future hybrid devices.

Experimental

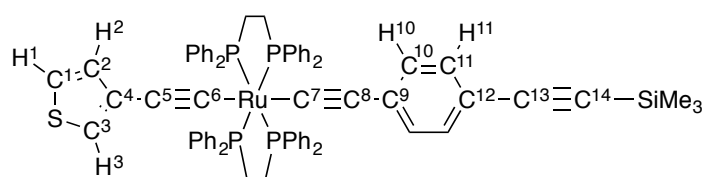
General conditions

All reactions were performed under an N₂ atmosphere using standard Schlenk techniques. Reaction solvents were purified and dried by standard methods, or from an inert solvent purification system. No special precautions were taken to exclude air or moisture during work-up. The compounds HC≡C-3-C₄H₃S,⁸⁶ HC≡C-1,4-C₆H₄-C≡CSiMe₃,⁵⁸ TIBF₄⁸⁷ and AuCl(PPh₃)⁸⁸ were prepared by literature routes, and *trans*-RuCl(C≡C-3-C₄H₃S)(dppe)₂ was prepared by deprotonation of the corresponding vinylidene complex.⁶⁴ NMR spectra were recorded in CDCl₃ solutions on Varian 300 MHz, Bruker Avance 500 MHz or 600 MHz spectrometers and referenced against residual protio-solvent resonances (CHCl₃: ¹H 7.26 ppm, ¹³C 77.16 ppm).⁸⁹ Infrared spectra were recorded on a Thermo 6700 spectrometer from CH₂Cl₂ solutions in a cell fitted with CaF₂ windows or an Agilent Technologies Cary 630 spectrometer using ATR sampling methods. High-resolution mass spectra were recorded using a Waters LCT Premier XE mass spectrometer using electrospray ionization or atmospheric pressure chemical ionisation with Leucine Enkephalin as reference.

SAFETY NOTE Given the extremely toxicity of TIBF₄, the reagent was weighed in a sealed container in a fume hood. The solid was transferred to the reaction flask using a disposable paper funnel. The paper funnel was discarded immediately after use into a thallium-containing solid waste receptacle. For larger scale reactions, a secondary containment flask was placed under the reaction vessel in case of

breakage during the reaction period. Reactions involving $TlBF_4$ produce $TlCl$, which is similarly extremely toxic. After completion of the reaction, following isolation of $TlCl$ / residual $TlBF_4$ by the work-up procedures reported, the salts were either disposed of by i) dissolving in HNO_3 (aq.) and transferring into a thallium-containing aqueous waste container or ii) in a thallium-containing solid waste container (along with the chromatographic medium, Celite etc.).

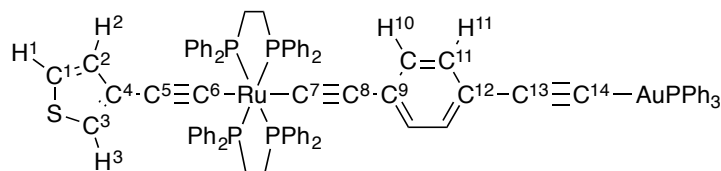
Preparation of *trans*- $Ru(C\equiv C-3-C_4H_3S)(C\equiv C-1,4-C\equiv CSiMe_3)(dppe)_2$ (**2**)



A solution of *trans*- $RuCl(C\equiv C-3-C_4H_3S)(dppe)_2$ (0.066g, 0.063 mmol), $HC\equiv C-1,4-C_6H_4-C\equiv CSiMe_3$ (0.013 g, 0.068 mmol), $TlBF_4$ (0.022 g, 0.076 mmol) in CH_2Cl_2 (7 ml) was treated with DBU (4 drops) and allowed to stir for 16 hours. The yellow solution colour lightened during this time and a white solid (presumably containing $TlCl$) precipitated. The solution was filtered through basic alumina, that had been previously dried in an oven overnight, to remove the solids (CARE) and the solvent removed from the yellow filtrate. The resulting solid was washed with diethyl ether (3 x 10 mL), hexanes (3 x 10 mL) and then air dried (0.057 g, 75%). IR (CH_2Cl_2/cm^{-1}): 2147 $\nu(C\equiv CSiMe_3)$, 2058 $\nu(RuC\equiv C)$. 1H NMR ($CDCl_3$, 600 MHz) δ / ppm: 0.27 (s, 9H, $SiMe_3$), 2.51 – 2.74 (m, 8H, CH_2 , dppe), 6.55 (d, $J_{HH} = 2$ Hz, 1H, H^3), 6.60 (apparent doublet, splitting = 8 Hz, 2H, H^{10}), 6.65 (d, $J_{HH} = 5$ Hz, 1H, H^2), 6.93 (t, $J_{HH} = 7$ Hz, 8H, H^{meta} , dppe), 6.98 (t, $J_{HH} = 7$ Hz, 8H, H^{meta} , dppe), 7.11 (dd, $J_{HH} = 5, 2$ Hz, 1H, H^1), 7.15 (t, $J_{HH} = 7$ Hz, 4H, H^{para} , dppe), 7.19 (t, $J_{HH} = 7$ Hz, 4H, H^{para} , dppe), 7.25 (apparent doublet, splitting = 8 Hz, 2H, H^{11}), 7.42 – 7.51 (m, 8H, H^{ortho} , dppe), 7.52 – 7.61 (m, 8H, H^{ortho} , dppe). $^{31}P\{^1H\}$ ($CDCl_3$, 300 MHz) δ / ppm: 54.5 (s, $Ru(dppe)_2$). $^{13}C\{^1H\}$ NMR ($CDCl_3$, 600 MHz) δ / ppm: 0.33 (s, $SiMe_3$), 31.6 (apparent t, splitting = 12 Hz, CH_2 , dppe), 93.7 (s, C^{14}), 106.3 (s, C^{13}), 111.3 (s, C^5), 116.6 (s, C^8), 117.3 (s, C^9), 120.5 (s, C^3), 122.9 (s, C^1), 127.1 (s, C^{meta} , dppe), 127.2 (s, C^{meta} , dppe), 127.8 (quin., $J_{CP} = 15$ Hz, C^6 or C^7), 128.7 (s, C^{para} ,

dppe), 128.8 (s, C^{para}, dppe), 129.87 (s, C¹⁰), 129.92 (s, C²), 130.3 (s, C⁴), 131.1 (s, C¹²), 131.4 (s, C¹¹), 134.3 (s, C^{ortho}, dppe), 134.5 (s, C^{ortho}, dppe), 136.7 – 137.1 (m, C^{ipso}, dppe), 137.1 – 137.4 (m, C^{ipso}, dppe), 138.9 (quin., $J_{CP} = 15$ Hz, C⁶ or C⁷). ESI(+)-MS (m/z): 1202 [Ru(C≡C-3-C₄H₃S)(C≡CC₆H₄-4-C≡CSiMe₃)(dppe)₂]⁺, 1136 [Ru(C≡CC₆H₄-4-C≡CSiMe₃)(dppe)₂ + MeCN]⁺, 1046 [Ru(C≡C-3-C₄H₃S)(dppe)₂ + MeCN]⁺, 1004 [Ru(C≡C-3-C₄H₃S)(dppe)₂ - H]⁺, 898 [Ru(dppe)₂]⁺. Anal. found: C, 70.42; H, 5.09. Calc. for C₇₁H₆₄P₄RuSSi: C, 70.87; H, 5.37 %. Crystals suitable for single-crystal X-ray diffraction were grown from CDCl₃ / MeOH at -18°C. Crystal data. C₇₂H₆₅Cl₃P₄RuSSi, $M = 1321.69$, triclinic, $a = 9.4433(5)$, $b = 13.3386(6)$, $c = 13.8508(6)$ Å, $\alpha = 77.282(4)$, $\beta = 74.659(4)$, $\gamma = 72.451(4)^\circ$, $U = 1585.38(13)$ Å³, $T = 100(2)$ K, space group $P\bar{1}$, 11994 reflections measured, 7035 unique ($R^{\text{int}} = 0.0436$), which were used in all calculations. The final $wR(F^2)$ was 0.1610 (all data).

Preparation of trans-Ru(C≡C-3-C₄H₃S)(C≡C-1,4-C≡CAuPPh₃)(dppe)₂ (3)



A solution of *trans*-Ru(C≡C-3-C₄H₃S)(C≡C-1,4-C≡CSiMe₃)(dppe)₂ (**2**) in a mixed solvent system of MeOH (5 mL), THF (10 mL) and CH₂Cl₂ (4 mL) was treated with NBu₄F·3H₂O (0.013 g, 0.048 mmol) and allowed to stir for 15 min. After this period, NaOH (0.017 g, 0.42 mmol) was added, and the solution stirred for a further 10 min, before addition of AuCl(PPh₃) (0.023 g, 0.45 mmol). The solution was stirred for a further 2 days. The solvents were removed in vacuum to give a yellow residue, which was extracted with CH₂Cl₂ and filtered through a short pad of alumina (basic, oven-dried). The pale yellow filtrate was taken to dryness to give a yellow solid, which was washed with MeOH (3 x 10 mL) and hexanes (3 x 10 mL) and air dried (0.060 g, 84%). IR (CH₂Cl₂/cm⁻¹): 2060 ν(C≡C), 2053

$\nu(\text{C}\equiv\text{C})$. ^1H NMR (CDCl_3 , 300 MHz) δ / ppm: 2.47 – 2.72 (m, 8H, CH_2 , dppe), 6.50 (d, $J_{\text{HH}} = 3$ Hz, 1H, H^3), 6.60 (apparent doublet, splitting = 8 Hz, 2H, H^{10}), 6.61 (d, $J_{\text{HH}} = 4$ Hz, 1H, H^2), 6.89 – 7.63 (m, 55H, Ph, dppe and PPh_3), 7.09 (dd, $J_{\text{HH}} = 4, 3$ Hz, 1H, H^1), 7.28 (apparent doublet, splitting = 8 Hz, 2H, H^{11}). $^{31}\text{P}\{^1\text{H}\}$ (CDCl_3 , 300 MHz) δ / ppm: 43.6 (s, AuPPh_3), 54.6 (s, $\text{Ru}(\text{dppe})_2$). $^{13}\text{C}\{^1\text{H}\}$ NMR (CDCl_3 , 600 MHz) δ / ppm: 31.4 – 32.0 (m, CH_2 , dppe), 111.2 (s, C^5 or C^8), 111.3 (s, C^5 or C^8), 120.4 (s, C^3), 122.8 (s, C^1), 127.1 (s, C^{meta} , Ph), 127.2 (s, C^{meta} , Ph), 128.7 (s, C^{para} , Ph), 128.8 (s, C^{para} , Ph), 129.27 (s, C^{para} , Ph), 129.33 (s, C^{para} , Ph), 130.0 (s, C^2), 131.7 (s, C^{10} or C^{11}), 131.8 (s, C^{10} or C^{11}), 134.2 – 134.8 (m, C^{ortho} , Ph), 136 – 137.8 (m, C^{ipso} , Ph). ESI(+)-MS (m/z): 898 $[\text{Ru}(\text{dppe})_2]^+$. Anal. found: C, 64.89; H, 4.26. Calc. for $\text{C}_{86}\text{H}_{70}\text{AuP}_5\text{RuS}$: C, 64.98; H, 4.44 %.

TIDOC nanoparticle formation

A SAM of **3** was prepared by incubating a Au(111), a QCM resonator or a Ag substrate in a 10^{-4} M solution of the complex in chloroform for 24 hours. After that, the substrate was rinsed copiously with chloroform to remove any physisorbed material, and dried under a stream of dry N_2 . Once the SAM of **3** was prepared, the surface supported SAM was annealed at 150 °C for two hours, and subsequently rinsed copiously with chloroform to remove any physisorbed material, and dried under a stream of dry N_2 . After this annealing process, GNPs were formed on top of the organometallic monolayer as it was demonstrated by atomic force microscopy (AFM) and X-ray photoelectron spectroscopy (XPS).

X-ray photoelectron spectroscopy (XPS) measurements.

X-ray photoelectron spectroscopy (XPS) spectra were acquired on a Kratos AXIS ultra DLD spectrometer with a monochromatic Al $\text{K}\alpha$ X-ray source (1486.6 eV) using a pass energy of 20 eV. The photoelectron take off angle was 90° with respect to the sample plane. To provide a precise energy calibration, the XPS binding energies were referenced to the C(1s) peak at 284.6 eV.

AFM experiments

Atomic force microscopy (AFM) experiments were performed using a Multimode 8 microscope equipped with a Nanoscope V control unit from Bruker. Tapping mode was used in ambient air conditions with a scan rate of 1 Hz with a silicon cantilever supplied by Bruker, RTESPA-150 (90-210 kHz, and 5 N·m⁻¹, and nominal tip radius of 8 nm).

Electrical measurements

Electrical properties of the metal-SAM-gold nanoparticles structures were determined with a conductive-AFM (Bruker ICON) under humidity control (ca. 40% by dry N₂ flux) using the Peak Force Tunnelling AFM (PF-TUNA™) mode. A PF-TUNA™ cantilever from Bruker (coated with Pt/Ir 20 nm, ca. 25 nm radius, 0.4 N·m⁻¹ spring constant and 70 kHz resonance frequency) was used and calibrated by thermal tuning method before each experiment.⁹⁰

Acknowledgements

P.C. is grateful for financial assistance from Ministerio de Economía y Competitividad from Spain and fondos FEDER in the framework of project MAT2016-78257-R. S.M. and P.C. acknowledge support from DGA/Fondos FEDER (construyendo Europa desde Aragón) for funding PLATON research group (E31_17R). S.G.E. held a Durham Doctoral Scholarship, further supported by the University of Western Australia. S.B. held a scholarship for doctoral studies from the University of Western Australia International Research Training Scholarship Program. P.J.L. gratefully acknowledges support from the Australian Research Council (DP140100855). The use of facilities, and the scientific and technical assistance of the Australian Microscopy & Microanalysis Research Facility at the Centre for Microscopy, Characterisation and Analysis, The University of Western Australia, a facility funded by the University, State and Commonwealth Governments, is acknowledged.

References

1. D. Xiang, X. L. Wang, C. C. Jia, T. Lee and X. F. Guo, *Chem Rev*, 2016, **116**, 4318-4440.
2. S. Marques-Gonzalez and P. J. Low, *Aust J Chem*, 2016, **69**, 244-253.
3. R. L. McCreery and A. J. Bergren, *Adv Mater*, 2009, **21**, 4303-4322.
4. R. L. McCreery, *Chem Mater*, 2004, **16**, 4477-4496.
5. T. A. Su, M. Neupane, M. L. Steigerwald, L. Venkataraman and C. Nuckolls, *Nat Rev Mater*, 2016, **1**, 1-15.
6. R. J. Nichols and S. J. Higgins, *Annu Rev Anal Chem*, 2015, **8**, 389-417.
7. Y. Komoto, S. Fujii, M. Iwane and M. Kiguchi, *J Mater Chem C*, 2016, **4**, 8842-8858.
8. S. V. Aradhya and L. Venkataraman, *Nat Nanotechnol*, 2013, **8**, 399-410.
9. C. Li, A. Mishchenko and T. Wandlowski, *Top Curr Chem*, 2012, **313**, 121-188.
10. R. J. Nichols, W. Haiss, S. J. Higgins, E. Leary, S. Martin and D. Bethell, *Phys Chem Chem Phys*, 2010, **12**, 2801-2815.
11. A. Vilan, D. Aswal and D. Cahen, *Chem Rev*, 2017, **117**, 4248-4286.
12. B. Branchi, F. C. Simeone and M. A. Rampi, *Top Curr Chem*, 2012, **313**, 85-119.
13. L. Wang, L. Wang, L. Zhang and D. Xiang, *Topics in Current Chemistry*, 2017, **375**.
14. W. Haiss, H. van Zalinge, S. J. Higgins, D. Bethell, H. Hobenreich, D. J. Schiffrin and R. J. Nichols, *J Am Chem Soc*, 2003, **125**, 15294-15295.
15. W. Haiss, H. van Zalinge, H. Hobenreich, D. Bethell, D. J. Schiffrin, S. J. Higgins and R. J. Nichols, *Langmuir*, 2004, **20**, 7694-7702.
16. W. Haiss, R. J. Nichols, H. van Zalinge, S. J. Higgins, D. Bethell and D. J. Schiffrin, *Phys Chem Chem Phys*, 2004, **6**, 4330-4337.
17. E. Tran, M. Duati, V. Ferri, K. Mullen, M. Zharnikov, G. M. Whitesides and M. A. Rampi, *Adv Mater*, 2006, **18**, 1323-1328.
18. M. A. Rampi and G. M. Whitesides, *Chem Phys*, 2002, **281**, 373-391.
19. R. C. Chiechi, E. A. Weiss, M. D. Dickey and G. M. Whitesides, *Angew Chem Int Ed*, 2008, **47**, 142-144.
20. W. Haiss, R. J. Nichols, S. J. Higgins, D. Bethell, H. Hobenreich and D. J. Schiffrin, *Faraday Discuss*, 2004, **125**, 179-194.
21. C. Chu, J. A. Ayres, D. M. Stefanescu, B. R. Walker, C. B. Gorman and G. N. Parsons, *J Phys Chem C*, 2007, **111**, 8080-8085.
22. G. Puebla-Hellmann, K. Venkatesan, M. Mayor and E. Lortscher, *Nature*, 2018, **559**, 232-235.
23. H. M. Osorio, P. Cea, L. M. Ballesteros, I. Gascon, S. Marques-Gonzalez, R. J. Nichols, F. Perez-Murano, P. J. Low and S. Martin, *J Mater Chem C*, 2014, **2**, 7348-7355.
24. L. Herrer, V. Sebastian, S. Martin, A. Gonzalez-Orive, F. Perez-Murano, P. J. Low, J. L. Serrano, J. Santamaria and P. Cea, *Nanoscale*, 2017, **9**, 13281-13290.
25. D. Y. Qu and K. Uosaki, *J Electroanal Chem*, 2011, **662**, 80-86.
26. S. Martin, G. Pera, L. M. Ballesteros, A. J. Hope, S. Marques-Gonzalez, P. J. Low, F. Perez-Murano, R. J. Nichols and P. Cea, *Chem Eur J*, 2014, **20**, 3421-3426.

27. S. Martin, L. M. Ballesteros, A. Gonzalez-Orive, H. Oliva, S. Marques-Gonzalez, M. Lorenzoni, R. J. Nichols, F. Perez-Murano, P. J. Low and P. Cea, *J Mater Chem C*, 2016, **4**, 9036-9043.
28. L. M. Ballesteros, S. Martin, J. Cortes, S. Marques-Gonzalez, F. Perez-Murano, R. J. Nichols, P. J. Low and P. Cea, *Adv Mater Interfaces*, 2014, **1**, 1400128.
29. R. Chico, E. Castillejos, P. Serp, S. Coco and P. Espinet, *Inorg Chem*, 2011, **50**, 8654-8662.
30. E. Castillejos, R. Chico, R. Bacsá, S. Coco, P. Espinet, M. Perez-Cadenas, A. Guerrero-Ruiz, I. Rodriguez-Ramos and P. Serp, *Eur J Inorg Chem*, 2010, 5096 - 5102.
31. S. J. Higgins and R. J. Nichols, *Polyhedron*, 2018, **140**, 25-34.
32. D. C. Milan, A. Vezzoli, I. J. Planje and P. J. Low, *Dalton Trans*, 2018, **47**, 14125-14138.
33. Y. Tanaka, M. Kiguchi and M. Akita, *Chem Eur J*, 2017, **23**, 4741-4749.
34. S. Rigaut, *Dalton Trans*, 2013, **42**, 15859-15863.
35. P. J. Low, *Dalton Trans*, 2005, 2821-2824.
36. L. Luo, A. Benameur, P. Brignou, S. H. Choi, S. Rigaut and C. D. Frisbie, *J Phys Chem C*, 2011, **115**, 19955-19961.
37. B. Kim, J. M. Beebe, C. Olivier, S. Rigaut, D. Touchard, J. G. Kushmerick, X. Y. Zhu and C. D. Frisbie, *J Phys Chem C*, 2007, **111**, 7521-7526.
38. X. P. Chen, M. Roemer, L. Yuan, W. Du, D. Thompson, E. del Barco and C. A. Nijhuis, *Nat Nanotechnol*, 2017, **12**, 797-803.
39. P. Song, L. Yuan, M. Roemer, L. Jiang and C. A. Nijhuis, *J Am Chem Soc*, 2016, **138**, 5769-5772.
40. L. Yuan, N. Nerngchamnong, L. Cao, H. Hamoudi, E. del Barco, M. Roemer, R. K. Sriramula, D. Thompson and C. A. Nijhuis, *Nat Commun*, 2015, **6**.
41. S. Pookpanratana, H. Zhu, E. G. Bittle, S. N. Natoli, T. Ren, C. A. Richter, Q. Li and C. A. Hacker, *J Phys Condens Mat*, 2016, **28**, 094009.
42. H. Zhu, S. J. Pookpanratana, J. E. Bonevich, S. N. Natoli, C. A. Hacker, T. Ren, J. S. Suehle, C. A. Richter and Q. L. Li, *Acs Appl Mater Inter*, 2016, **8**, 19842-19842.
43. H. Zhu, S. J. Pookpanratana, J. Y. Bonevich, S. N. Natoli, C. A. Hacker, T. Ren, J. S. Suehle, C. A. Richter and Q. L. Li, *ACS Appl Mater Inter*, 2015, **7**, 27306-27313.
44. S. Pookpanratana, I. Savchenko, S. N. Natoli, S. P. Cummings, L. J. Richter, J. W. F. Robertson, C. A. Richter, T. Ren and C. A. Hacker, *Langmuir*, 2014, **30**, 10280-10289.
45. A. K. Mahapatro, J. W. Ying, T. Ren and D. B. Janes, *Nano Lett*, 2008, **8**, 2131-2136.
46. K. Sugimoto, Y. Tanaka, S. Fujii, T. Tada, M. Kiguchi and M. Akita, *Chem Commun*, 2016, **52**, 5796-5799.
47. K. Liu, X. H. Wang and F. S. Wang, *ACS Nano*, 2008, **2**, 2315-2323.
48. T. Ren, D. A. Parish, G. L. Xu, M. H. Moore, J. R. Deschamps, J. W. Ying, S. K. Pollack, T. L. Schull and R. Shashidhar, *J Organomet Chem*, 2005, **690**, 4734-4739.
49. M. Mayor, C. von Hanisch, H. B. Weber, J. Reichert and D. Beckmann, *Angew Chem Int Ed*, 2002, **41**, 1183-1186.

50. T. L. Schull, J. G. Kushmerick, C. H. Patterson, C. George, M. H. Moore, S. K. Pollack and R. Shashidhar, *J Am Chem Soc*, 2003, **125**, 3202-3203.
51. F. Schwarz, G. Kastlunger, F. Lissel, C. Egler-Lucas, S. N. Semenov, K. Venkatesan, H. Berke, R. Stadler and E. Lortscher, *Nat Nanotechnol*, 2016, **11**, 170-176.
52. F. Schwarz, G. Kastlunger, F. Lissel, H. Riel, K. Venkatesan, H. Berke, R. Stadler and E. Lortscher, *Nano Lett*, 2014, **14**, 5932-5940.
53. F. Lissel, F. Schwarz, O. Blacque, H. Riel, E. Lortscher, K. Venkatesan and H. Berke, *J Am Chem Soc*, 2014, **136**, 14560-14569.
54. Y. Tanaka, Y. Kato, T. Tada, S. Fujii, M. Kiguchi and M. Akita, *J Am Chem Soc*, 2018, **140**, 10080-10084.
55. S. Bock, O. A. Al-Owaedi, S. G. Eaves, D. C. Milan, M. Lemmer, B. W. Skelton, H. M. Osorio, R. J. Nichols, S. J. Higgins, P. Cea, N. J. Long, T. Albrecht, S. Martin, C. J. Lambert and P. J. Low, *Chem Eur J*, 2017, **23**, 2133-2143.
56. O. A. Al-Owaedi, S. Bock, D. C. Milan, M. C. Oerthel, M. S. Inkpen, D. S. Yufit, A. N. Sobolev, N. J. Long, T. Albrecht, S. J. Higgins, M. R. Bryce, R. J. Nichols, C. J. Lambert and P. J. Low, *Nanoscale*, 2017, **9**, 9902-9912.
57. O. A. Al-Owaedi, D. C. Milan, M. C. Oerthel, S. Bock, D. S. Yufit, J. A. K. Howard, S. J. Higgins, R. J. Nichols, C. J. Lambert, M. R. Bryce and P. J. Low, *Organometallics*, 2016, **35**, 2944-2954.
58. S. Marques-Gonzalez, D. S. Yufit, J. A. K. Howard, S. Martin, H. M. Osorio, V. M. Garcia-Suarez, R. J. Nichols, S. J. Higgins, P. Cea and P. J. Low, *Dalton Trans*, 2013, **42**, 338-341.
59. F. B. Meng, Y. M. Hervault, Q. Shao, B. H. Hu, L. Norel, S. Rigaut and X. D. Chen, *Nat Commun*, 2014, **5**, 3023.
60. X. Y. He, C. Lagrost, L. Norel and S. Rigaut, *Polyhedron*, 2018, **140**, 169-180.
61. C. R. Arroyo, S. Tarkuc, R. Frisenda, J. S. Seldenthuis, C. H. M. Woerde, R. Eelkema, F. C. Grozema and H. S. J. van der Zant, *Angew Chem Int Ed*, 2013, **52**, 3152-3155.
62. M. A. Fox, J. E. Harris, S. Heider, V. Perez-Gregorio, M. E. Zakrzewska, J. D. Farmer, D. S. Yufit, J. A. K. Howard and P. J. Low, *J Organomet Chem*, 2009, **694**, 2350-2358.
63. N. Gauthier, N. Tchouar, F. Justaud, G. Argouarch, M. P. Cifuentes, L. Toupet, D. Touchard, J. F. Halet, S. Rigaut, M. G. Humphrey, K. Costuas and F. Paul, *Organometallics*, 2009, **28**, 2253-2266.
64. K. Sugimoto, H. Idei, Y. Tanaka and M. Akita, *J Organomet Chem*, 2017, **847**, 121-131.
65. S. Marques-Gonzalez, M. Parthey, D. S. Yufit, J. A. K. Howard, M. Kaupp and P. J. Low, *Organometallics*, 2014, **33**, 4947-4963.
66. R. J. Cross and M. F. Davidson, *J Chem Soc Dalton Trans*, 1986, 411-414.
67. G. Sauerbrey, *Z Phys*, 1959, **155**, 206-222.
68. A. Gulino, *Anal Bioanal Chem*, 2013, **405**, 1479-1495.
69. D. Briggs and J. T. Grant, *Surface analysis by Auger and X-ray photoelectron spectroscopy*, IMP, Chichester, 2003.
70. S. Kato, M. Kivala, W. B. Schweizer, C. Boudon, J. P. Gisselbrecht and F. Diederich, *Chem Eur J*, 2009, **15**, 8687-8691.
71. W. M. Khairul, D. Albesa-Jove, D. S. Yufit, M. R. Al-Haddad, J. C. Collings, F. Hartl, J. A. K. Howard, T. B. Marder and P. J. Low, *Inorg Chim Acta*, 2008, **361**, 1646-1658.

72. Y. M. Liu, H. Tsunoyama, T. Akita and T. Tsukuda, *J Phys Chem C*, 2009, **113**, 13457-13461.
73. K. Guillois, L. Burel, A. Tuel and V. Caps, *Appl Catal A*, 2012, **415**, 1-9.
74. T. Matsushita, Y. Fukumoto, T. Kawakami, T. Tsuruoka, T. Murashima, T. Yanagishita, H. Masuda, H. Nawafune and K. Akamatsu, *RSC Adv*, 2013, **3**, 16243-16246.
75. M. K. Bayazit, S. A. Hodge, A. J. Clancy, R. Menzel, S. Chen and M. S. P. Shaffer, *Chem Commun*, 2016, **52**, 1934-1937.
76. V. V. Agrawal, G. U. Kulkarni and C. N. R. Rao, *J Phys Chem B*, 2005, **109**, 7300-7305.
77. E. Aguilo, R. Gavara, J. C. Lima, J. Llorca and L. Rodriguez, *J Mater Chem C*, 2013, **1**, 5538-5547.
78. I. Fratoddi, I. Venditti, C. Battocchio, G. Polzonetti, C. Cametti and M. V. Russo, *Nanoscale Res Lett*, 2011, **6**.
79. G. Z. Liu, E. Luais and J. J. Gooding, *Langmuir*, 2011, **27**, 4176-4183.
80. J. Canet-Ferrer, E. Coronado, A. Forment-Aliaga and E. Pinilla-Cienfuegos, *Nanotechnology*, 2014, **25**.
81. A. Moneo, A. Gonzalez-Orive, S. Bock, M. Fenero, I. L. Herrero, D. C. Milan, M. Lorenzoni, R. J. Nichols, P. Cea, F. Perez-Murano, P. J. Low and S. Martin, *Nanoscale*, 2018, **10**, 14128-14138.
82. B. Pittenger, N. Erina and C. Su, *Application Note #128: Quantitative Mechanical Property Mapping at the Nanoscale with PeakForce QNM*, 2012, Bruker Nano Surfaces Division.
83. C. T. Gibson, D. A. Smith and C. J. Roberts, *Nanotechnology*, 2005, **16**, 234-238.
84. M. Araidai and M. Tsukada, *Phys Rev B*, 2010, **81**.
85. A. Vilan, D. Cahen and E. Kraiser, *ACS Nano*, 2013, **7**, 695-706.
86. D. Solooki, J. D. Bradshaw, C. A. Tessier and W. J. Youngs, *Organometallics*, 1994, **13**, 451-455.
87. F. J. Arnaiz, *J Chem Ed*, 1997, **74**, 1332-1333.
88. M. I. Bruce, B. K. Nicholson, O. Binshawkataly, J. R. Shapley and T. Henly, *Inorg Synth*, 1989, **26**, 324-328.
89. G. R. Fulmer, A. J. M. Miller, N. H. Sherden, H. E. Gottlieb, A. Nudelman, B. M. Stoltz, J. E. Bercaw and K. I. Goldberg, *Organometallics*, 2010, **29**, 2176-2179.
90. J. P. Cleveland, S. Manne, D. Bocek and P. K. Hansma, *Rev Sci Instrum*, 1993, **64**, 403-405.